

## **Effect of welding polarity on bead geometry, microstructure, microhardness, and residual stresses of 1020 steel**

ABDULKAREEM ALORAIE\*, KHALED AL-FADHALAH\*\*, ANNA M. PARADOWSKA\*\*\*, EMAD ALFARAJ\*\*\*\*

*\*Department of Manufacturing and Welding Technology, College of Technological Studies, PAAET, Kuwait*

*\*\*Department of Mechanical Engineering, College of Engineering & Petroleum, Kuwait University, Kuwait*

*\*\*\*The Bragg Institute, Australian Nuclear Science and Technology Organisation, Australia*

*\*\*\*\*Department of Mechanical Engineering, Gulf University, Kingdom of Bahrain*

### **ABSTRACT**

This work examines the effect of welding polarity as a measure of heat input on the bead geometry, microstructure, microhardness and residual stresses of AISI 1020 carbon steel that was processed by shielded metal arc welding (SMAW). Single weld beads were deposited on the steel plate using a constant current but with different welding polarities of AC, DC- and DC+. Optical microscopy indicates that welding by DC- provides the widest weld bead and largest heat affected zone (HAZ) due to the large heat input subjected to the plate. Nevertheless, similar microstructures in the HAZ and fusion zone (FZ) of the weld were found for all welding polarities. Vickers microhardness tests also show that the large heat input by DC- polarity provided the minimum microhardness for all microstructures of the weld. In addition, across-weld measurements of the residual stresses by neutron diffraction indicate that the three welding polarities produced similar profile. High tensile longitudinal residual stresses were found to extend horizontally from the weld center to the HAZ, which become compressive further away from the bead. The highest tensile residual stress in the HAZ occurred for DC- polarity, while it has the lowest value for AC polarity. Through-thickness measurements also indicate that the residual stresses within the HAZ are approximately constant for AC polarity. This suggests that equal distribution of heat input by AC polarity to the electrode and plate is not only important for reducing residual stresses but also on minimizing the differences in residual stresses through the weld thickness.

**Keywords:** Bead geometry; hardness; microstructure; residual stresses; welding polarity.

## NOMENCLATURE

A1	Lower Critical Temperature
A3	Upper Critical Temperature
AC	Alternating Current
DC-	Direct Current Negative Polarity
DC+	Direct Current Positive Polarity
FCAW	Flux Cored Arc Welding
FZ	Fusion Zone
GMAW	Gas Metal Arc Welding
GTAW	Gas Tungsten Arc Welding
HAZ	Heat Affected Zone
ND	Neutron Diffraction
OM	Optical Microscopy
PAW	Plasma Arc Welding
SMAW	Shielded Metal Arc Welding

## INTRODUCTION

Shielded metal arc welding (SMAW) is a manual arc welding process that has a number of advantages over other welding processes, such as being simple, portable and requiring inexpensive equipment. In SMAW, the heat for welding is generated by an arc established between a flux-covered consumable electrode and the workpiece. The core wire conducts the electric current to the arc and provides filler metal for the joint. The heat of the arc melts the core wire and the flux covering at the electrode tip into metal droplets. Molten metal in the fusion zone (FZ) solidifies into the weld metal while the lighter molten flux floats on the top surface and solidifies as a slag layer. The weld area is protected by a gaseous shield obtained from the combustion of the flux. Additional shielding is provided by the slag. A small amount of the weld is deposited in each pass and, thus, the process of SMAW is labor-intensive. Regardless, it is widely used due to its versatility in joining, enhanced wear resistance coating, maintenance, and remote welding repair (Messler, 2004).

There are three welding polarities commonly employed when using SMAW. The polarity, in general, depends on the power supply being used. If a direct current power supply is used and the workpiece is connected to the positive terminal, the polarity is referred to as straight polarity (DCSP), also sometimes called direct current electrode

negative (DC-). On the other hand, if the workpiece is connected to the negative terminal of a direct current power supply, the polarity is referred to as direct current reverse polarity (DCRP) or sometimes called direct current electrode positive (DC+). If an alternating current power supply is used, the polarity is referred to as AC. In DC-, about 70% of the heat is directed to the workpiece and 30% of the heat is directed to the electrode, and vice versa when DC+ polarity is used. In AC polarity, about 50% of the heat is directed to the workpiece and the other 50% of the heat is directed to the electrode. The difference in heat distribution results in varying of the weld bead geometry. DC- polarity usually produces a narrow and deep FZ due to the high energy in the parent metal. Furthermore, the arc forces the droplets away from the workpiece due to the low rate of electron emission from the negative electrode. On the other hand, DC+ polarity usually results in shallow FZ. Welding with DC+ polarity can be used to clean the surface of the workpiece as the positive ions of the shielding gas knock off oxide films. The AC polarity provides reasonably good penetration of the FZ and oxide cleaning (Kou, 2003). As the DC+ polarity results in more heat being supplied to the electrode, it is recommended for arc processes that employ consumable electrodes, such as SMAW, GMAW and FCAW. On the contrary, DC- polarity is advisable for welding processes that employ non-consumable electrodes such as GTAW and PAW, since less heat is directed to the electrode.

The weld quality when using the SMAW process can be affected by several welding parameters, such as arc-length, electrode type, metal deposition, arc-travel rate and welding polarity (Messler, 2004; Chandel et al., 1997). In particular, these factors have control over the bead geometry, depth of penetration and heat affected zone (HAZ) profiles. Apps et al. (1963) reported that several arc welding parameters, such as current, voltage, welding speed, and polarity can influence the bead shape and size. In addition, it has been demonstrated that the depth of penetration is influenced by polarity, current, voltage and arc-travel rate (Jefferson, 1951; Jackson, 1960; Gill and Simons, 1950). Moreover, some researchers (Chandel et al., 1997; Yang et al., 1992; Nagesh and Datta, 2002) considered welding polarity as a primary factor influencing the SMAW process. The importance of the polarity arises mainly from the difference in the amount of heat input into the workpiece. Changing the polarity affects the amount of heat in the weld zone and, thus, alters the bead geometry, depth of penetration, and HAZ profiles. It also affects the heterogeneity of the microstructure and causes gradient of properties in the parent metal and the HAZ. In the case of high heat input, retention of heat might occur in the welded joint and, hence, lower the hardness of welded metal and its HAZ.

Moreover, residual stresses are commonly formed in the weld region. This is primarily due to the differences in temperature distribution and/or microstructure of the weld and parent metal during heating and cooling cycles. Residual stresses

are known to lower the performance of welded components (Webster and Wimpory, 2001). There are several ways of measuring residual stresses in welded components. The most common ones involve mechanical invasive methods, such as hole drilling (Pang et al., 2003; Jang et al., 2003), and non-destructive methods using radiation, such as x-ray (synchrotron) or neutron diffraction (ND) (Webster et al., 2002; Owen et al., 2003; Lorentzen and Ibs, 1995). In general, ND can obtain residual stresses non-destructively within the subsurface and deep within the bulk of the components. Neutrons can evaluate the weld structure in three principal directions, with high spatial resolution of 1 mm (or less) to a depth of many millimeters below the weld surface (up to 50 mm for steel). An international standard (ISO/TTA 3, 2001; D.C.I.T. 21432, 2005) for measuring residual stresses using ND is being developed on a ring plug fit to achieve reproducible and reliable stress measurements. ND was successfully applied to evaluate residual stresses in several welding components. Researchers have used the neutron diffraction technique to investigate and compare the residual stress characteristics due to various restraints for a single bead and in fully restrained samples with different numbers of beads (Price et al., 2006, 2008; Paradowska et al., 2005, 2006, 2006).

At this moment, there is no agreement on how to reduce the amount of tensile residual stress in the weld by altering the amount of heat input. Also, a cross-correlation among residual stresses, hardness and microstructure in metal welds has not been fully developed. Therefore, the current study aims to investigate the effect of welding polarity on single-bead geometry, microstructure, microhardness and residual stresses of 1020 steel produced by SMAW.

## EXPERIMENTAL WORK

A constant AC/DC current welding power source was used in this experimental work. Welding electrodes conforming to AWS E6013 with diameter and length of 5.0 mm x 400 mm were used to make bead-on-plate welds. The parent metal plate used in this experimental work was AISI 1020 carbon steel with dimensions of 200×100×10 mm<sup>3</sup>. The chemical composition of the parent metal and electrode is shown in Table 1.

**Table 1.** Chemical composition (in wt%) of the parent metal and welding electrode.

Elements	C	Si	Mn	P	S	Cr	Ni	Cu	Ni
Parent metal (1020 Steel)	0.196	0.2	0.577	0.013	0.007	0.043	0.049	0.07	0.012
Weld electrode (AWS E6013)	0.12	0.35	0.3- 0.6	0.04	0.035	---	---	---	---

The bead was deposited in the center of the plate so that it would start and end 25 mm from each side of the plate. Figure 1 shows a schematic of the dimensions of the bead and the plate, and elements of the bead geometry. Microstructural examinations were carried out on cross-sectional samples of the weldment. The samples were cold-mounted, ground and polished using a standard metallographic technique, before etching in a 2% nital solution. Stereo and optical microscopy were used to evaluate the bead geometry and the microstructure of the weld metal, the heat affected zone and the parent metal. In addition, Vickers microhardness (Hv) tests were employed to measure the variation of hardness across the weld zone. All samples were mechanically ground and polished prior to making microhardness indentations. The indentations were made with a load of 200 gf and dwell time of 15 sec, with 0.5 mm intervals taken between measurements. Horizontal measurements of the hardness of the weld were made at different distances below the top surface of the plate, i.e. 0.5, 1, and 1.5 mm. Also, vertical hardness measurements were taken through the sample thickness at the center of the weld, starting from the bottom surface of the plate to the top of the weld bead. Vertical measurements were made at 0, -0.5, and 0.5 mm from the center. For both types of microhardness measurements, the microstructures in which the indentations were made were identified with the help of OM.

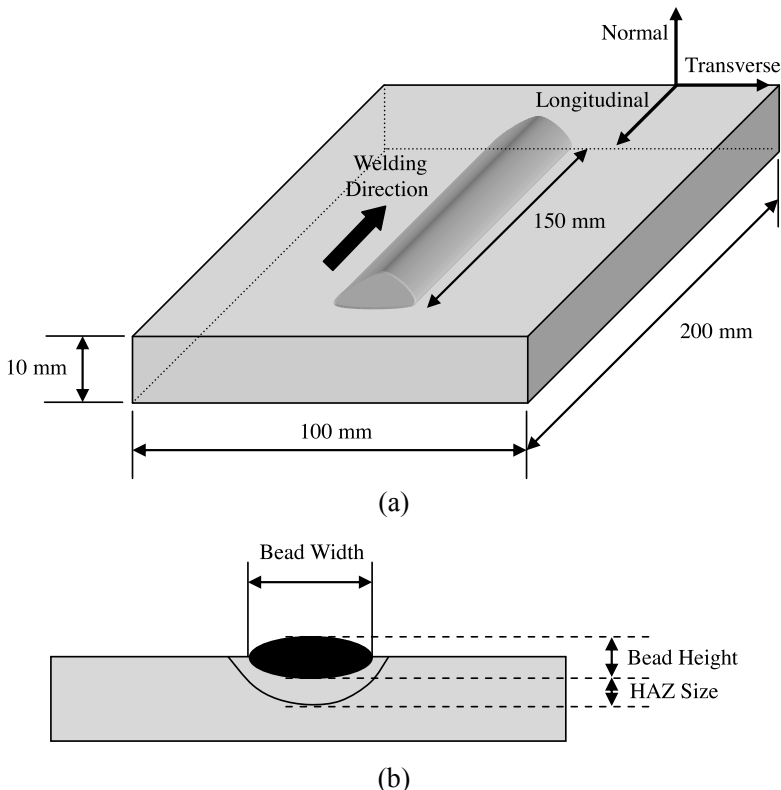


**Fig. 1.** Illustration of (a) bead dimensions and (b) bead geometry elements.

The residual strain/stress measurements were performed on the ENGIN-X beam-line at ISIS, UK. Fig. 2(a) shows a schematic of the data collection on ENGIN-X (ISO/TTA 3, 2001). On ENGIN-X, one can define a small measurement volume (gauge volume) in the sample in the order of a few cubic millimeters. This is achieved by collimating the incident beam (width x height), and by using a radial collimator in front of the detectors to accept only neutrons from a certain depth along the incident beam direction, as can be seen in Fig. 2(a). As ENGIN-X utilizes a spallation neutron source, it is a time-of-flight facility, and multiple diffraction peaks were acquired simultaneously. This enabled the lattice parameter to be obtained directly using a Pawley-Rietveld refinement of a time-of-flight profile. For the longitudinal and reference sample measurements, the gauge volume was  $2 \times 2 \times 2 \text{ mm}^3$ , but for the transverse and normal measurements, this gauge volume could be relaxed in the vertical direction to obtain the volume of  $2 \times 2 \times 10 \text{ mm}^3$ . The reference sample for “stress free” value was extracted from the parent metal plate, cut from the corner of the sample ( $4 \times 4 \times 4 \text{ mm}^3$ ) using an electro-discharging machine. The longitudinal, transverse and normal components of the residual stress field were calculated for each strain-measurement position in the weldment from the relevant three strain components. This was done using standard elasticity theory, assuming an elastically isotropic material and that the measurement directions correspond to the principal axes of the stress tensor. For this conversion, a Young’s modulus of 207 GPa and Poisson’s ratio of 0.3 were used.

The focus of this work was on the detailed line scans across the weld 2 mm below the surface (because of the symmetry of the specimens, the measurements were carried out only on one half) and through the thickness of the plate in the middle of the weldments. Neutron beam measurements, as illustrated in Fig. 2(b), were made horizontally 2 mm below the top surface, and vertically in the middle of the weld through the thickness of the plate.

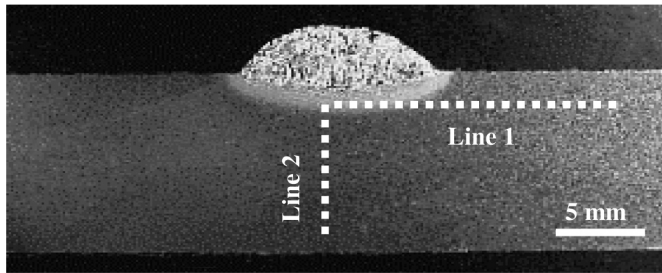
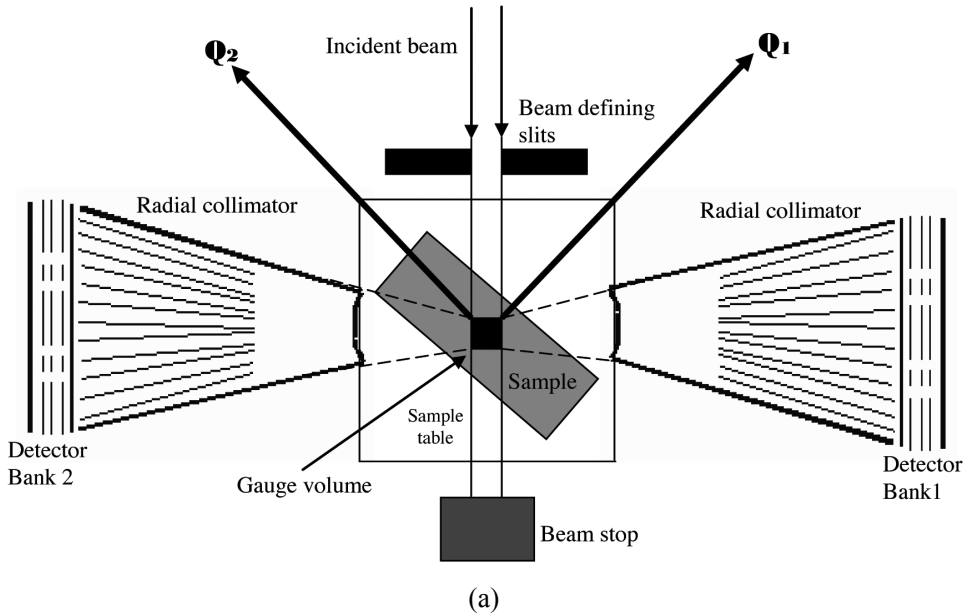


**Fig. 2.** (a) Schematic of the data collection on ENGIN-X [16]. (b) Illustration showing the location of neutron measurements. Line (1) represents measurements taken 2 mm below the surface and line (2) demonstrates measurements in the middle of the weld through the plate thickness.

## RESULTS AND DISCUSSION

### Bead geometry

Figure 3 shows the bead geometry of the weld samples for the three polarity conditions. Table 2 also presents the average measurements of bead geometry in terms of total height, weld bead width, FZ height, and HAZ size. The results indicate that the sample with DC- polarity has the maximum bead width of 15.44 mm and maximum HAZ size of 4.43 mm, while it has a minimum bead height of 3.52 mm. On the other hand, DC+ and AC polarity samples have similar total height of 12.6 mm and bead width of 12.9 mm. However, the DC+ polarity sample is characterized by a larger bead height of 3.86 mm and a smaller HAZ, as compared to the AC polarity sample. The bead width-to-depth ratio is also calculated in Table 2.

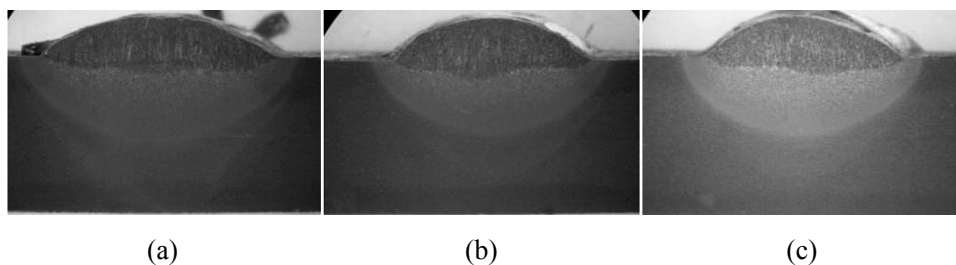


**Fig. 3.** Macrographs of the weldment samples of different polarities (a) DC-, (b) DC+, and (c) AC.

**Table 2.** Average measurements of bead geometry for samples of different welding polarities.

Polarity	Total Height (mm)	Bead Width (mm)	Bead Depth (mm)	HAZ Size (mm)	Bead Width-to-Depth Ratio
DC-	12.31	15.44	3.52	4.43	4.39
DC+	12.60	12.91	3.86	3.54	3.34
AC	12.64	12.86	3.57	3.98	3.60

It is an important parameter for assessing the quality of a welded joint in terms of the fusion area and percentage of dilution, where the latter is defined as the weight of the parent metal melted divided by the total weight of the weld metal (Chakravarti et al., 1985). The results show that the DC- polarity sample has the largest ratio (4.39) and, hence, has the highest dilution, causing more melting in the parent metal. In general, the results suggest that the maximum heat input to the parent metal during welding was for the DC- polarity sample, followed by the AC polarity sample, and least to the DC+ polarity sample.



## **Weld microstructure**

All weld samples were generally observed to have similar microstructures in the weld zone. As a result, the variation of microstructure through the weld is only described for the DC+ polarity sample, as shown in Figure 4. In general, there are six distinct regions that have been identified. As shown in Fig. 4(a), region 1 represents the unaffected microstructure of the parent metal containing ferritic and pearlitic grains in a cold-rolled condition. In region 2 (Fig. 4b), the microstructure is slightly affected by heating in the intercritical region of HAZ, i.e. heating between the  $A1$  and  $A3$  temperatures. The  $A3$  represents the upper critical temperature below which ferrite starts to form as a result of ejection from austenite, while  $A1$  denotes the lower critical temperature below which the austenite-to-pearlite transformation occurs. Fig. 4b shows that the pearlite colonies became much finer due to the heating into the critical range, in which the pearlite transformed into austenite and back into pearlite upon subsequent cooling; many of the ferrite grains remained unchanged. Fig. 4(c) represents region 3, in which grain refinement occurred. In this fine-grained region of HAZ, the material was heated to just above  $A3$ , forming fine grain austenite that reverted quickly to fine pearlite and ferrite structure. Region 4 (Fig. 4d) shows the microstructure of HAZ near to the fusion line, which has large grains that consist of ferrite phase at the grain boundaries and coarse pearlite in the interior. Formation of Widmanstätten ferrite, as shown by the growth of ferrite side-plates from the grain boundaries, is also observed. For the coarse-grained region of HAZ, the material was heated well above  $A3$ , resulting in grain growth of the austenitic phase that later changed to coarse pearlitic structure upon cooling. Moreover, the microstructure of the FZ identified by regions 5 and 6 is shown in Figs. 4(e) and (f).

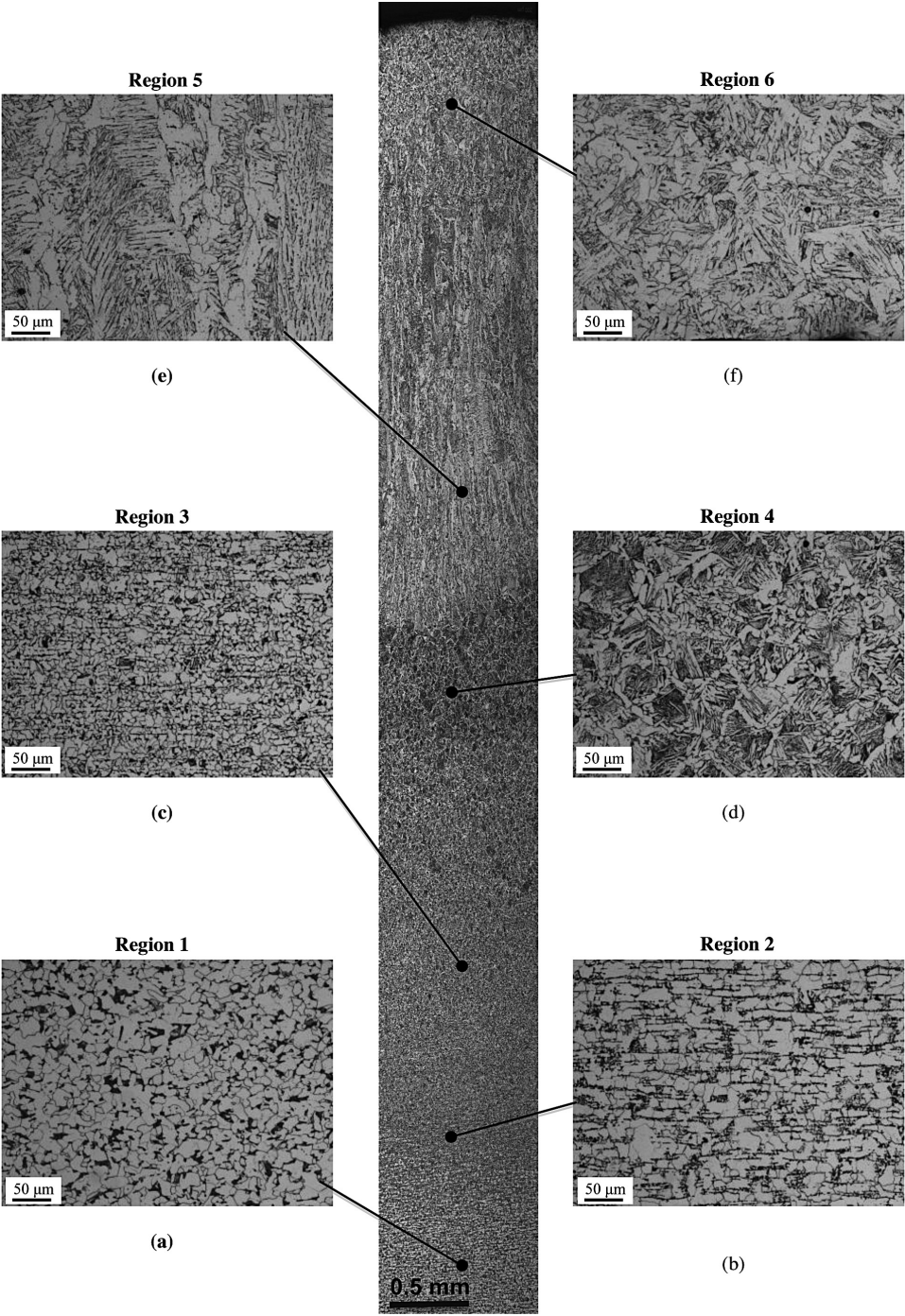
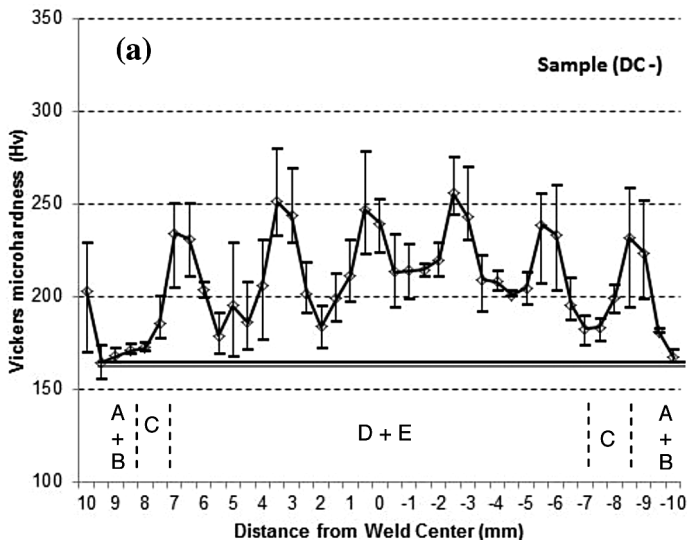


**Fig. 4.** Microstructures of DC+ polarity sample at different regions.

Due to the grain coarsening in the HAZ near the fusion boundary, coarse columnar dendrites at the fusion line were formed in region 5. The columnar growth extended inward to the center of the FZ, having dendrites larger than the HAZ grains on average. Region 6 represents the upper region of the FZ that is made of equiaxed dendrites. The microstructure of the FZ mainly consists of acicular ferrite, grain boundary ferrite, and Widmanstätten ferrite. There is no sign of bainite or martensite phases being formed in the FZ. The microstructural development of low carbon steel welds was examined by (Samuels, 1980), who indicated that a significant amount of Widmanstätten ferrite forms when an appreciable under-cooling below the *A1* temperature occurs during solidification of the weld. It was also indicated that the structural constituents that form in the HAZ depend on the composition of the parent metal. For a steel alloy of small carbon content, such as in the current study, the HAZ zone would be mostly pearlitic with some proeutectoid ferrite, i.e. grain boundary ferrite and Widmanstätten ferrite. Samuels also added that the formation of martensitic structure rarely occurs for steel with low carbon content (Samuels, 1980).

### Microhardness

Figure 5 presents the average microhardness profile computed from indentation points measured horizontally across the weld. The measurements were made at different distances below the top surface of the plate (0.5, 1, and 1.5 mm). The microstructure in which the indentations were made was identified and the OM observations indicate the microhardness measurements were made in the parent metal, HAZ, and the bottom of FZ near to the fusion line. The microhardness of the parent metal was measured for twenty points far from the weld zone, having an average of  $165 \pm 5$  Hv, as presented by a solid line in Figure 5.



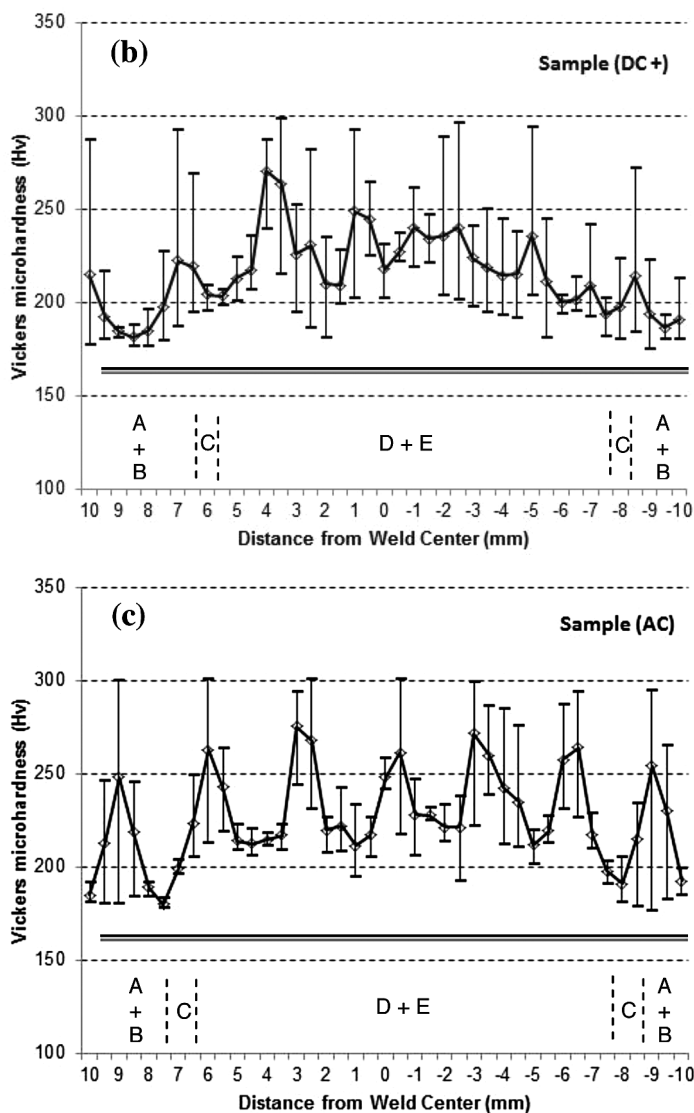
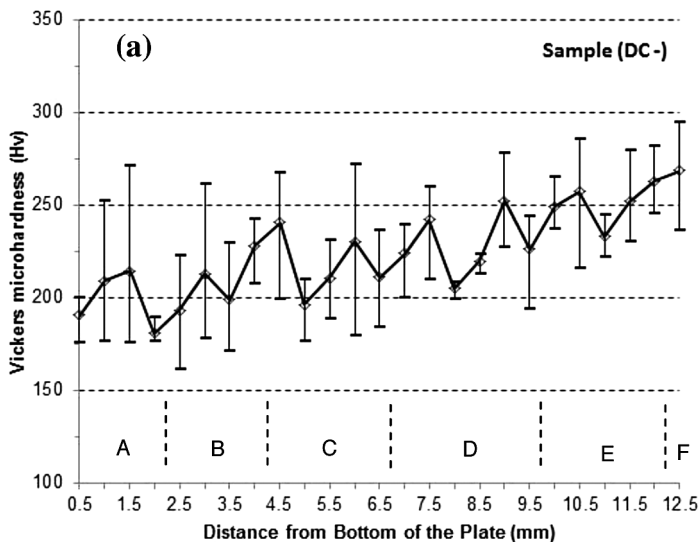


**Fig. 5.** Horizontal profile of the microhardness across the weld for samples welded by: (a) DC- polarity, (b) DC+ polarity, and (c) AC. The letters denotes the microstructure in which the indentation was made as follows: A: Parent Metal, B: Inter-critical HAZ, C: fine-grained HAZ, D: coarse-grained HAZ, and E: large and long dendrites of FZ.

In addition, all samples show similar microhardness profiles of alternating hardness across the HAZ, with maximum value at the weld center and minimum value at the parent metal. In general, the variation in microhardness may arise from the difference in grain size, difference in temperature during heating and cooling cycles, and difference in hardness between ferritic and pearlitic phases. The alternating tendency of the microhardness across the HAZ is strongly shown for DC- and AC samples, and

less likely for the DC+ sample. It can also be observed that the highest microhardness values in the HAZ are found for AC and DC+ samples, while the lowest hardness values were recorded for the sample of DC- polarity. This indicates that the large heat input by DC- polarity provided longer thermal cycles of the welding process and, thus, coarser and softer microstructures.

Moreover, the microhardness profile is recorded vertically (through thickness) at the center of the weld, as shown in Figure 6, starting from the bottom surface of the plate to the top of the weld bead. The DC- polarity sample has the minimum hardness values in most measurements, particularly in the HAZ, as compared to DC+ and AC polarity samples. Also, it can be observed that by changing the welding polarity, a different amount of heat was produced, which in return affected the depth of the HAZ and, consequently, the microhardness. As shown in Figure 6, the intercritical region of the HAZ reaches a depth of 2 mm from the bottom of the plate for the DC- polarity sample, while it is 2.5 mm for DC+ and AC polarity samples. In addition, a remarkable increase in the microhardness is shown for all samples at a distance of 5–12.5 mm from the bottom of the plate. In general, this corresponds to three regions: fine-grained HAZ, coarse-grained HAZ, and FZ. The high level of hardness in these regions occurred for different reasons. In the fine-grained region of the HAZ, fine pearlitic and ferritic structures (Fig. 4c) were formed resulting in an increase in the hardness by grain size reduction.



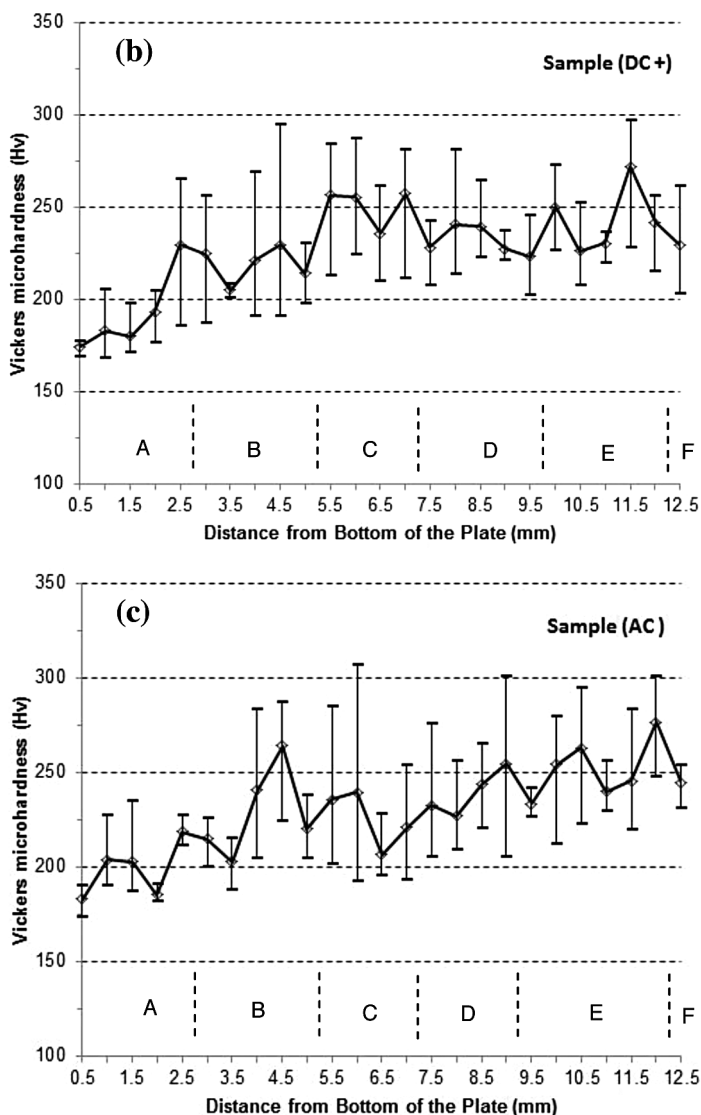


**Fig. 6.** Vertical profile of the microhardness at the weld center for samples welded by: (a) DC- polarity, (b) DC+ polarity, and (c) AC. The letters denotes the microstructure in which the indentation was made; A: Parent Metal, B: Intercritical HAZ, C: fine-grained HAZ, D: coarse-grained HAZ, E: large and long dendrites of FZ, and F: equiaxed dendritic grains of FZ.

On the other hand, the formation of Widmanstätten ferrite and coarse pearlite microstructure in the HAZ close to FZ (Fig. 4d) contributed to the increase in hardness. Within the FZ, the presence of the hard acicular ferrite and the Widmanstätten ferrite microstructure (Fig. 4e) has maintained the microhardness at values higher than that for the PM. Moreover, the microhardness across the weld samples, in this study, is in the range of 165-305 Hv, which is sufficiently lower than that required to widely form

hard phases of bainite or martensite. This confirms that during the welding cooling cycle, the undercooling occurred near the  $A1$  temperature for all regions of the HAZ and, hence, pearlitic transformation was promoted rather than bainitic or martensitic transformation (Elmer & Palmer, 2006).

Figure 7 shows statistical distribution (using box plot) of the microhardness for the different microstructures found in each weld sample. The lower boundary of the box indicates the 25th percentile, while the upper boundary of the box represents the 75th percentile; a line within the box marks the median and the error bars above and below the box indicate the 90th and 10th percentiles, respectively. In general, the microhardness median increases gradually from PM and reaches its maximum in the coarse-grained region of the HAZ, and then remains at the same level in the FZ. It is also interesting to note that the median of microhardness is the highest for the AC polarity sample and lowest for DC- polarity sample regardless to the type of microstructure. This indicates that changing the amount of heat absorbed by the plate, through applying different welding polarities, affects not only the microstructure evolution but also the microhardness values within each type of microstructure. Thus, the results suggest that more time was needed to cool down the plate in the case of DC- polarity due to the large amount of energy being applied, which caused further softening of each microstructure after formation. In addition, the large amount of energy applied to the electrode as in the case of DC+ polarity will also affect the microhardness distribution, resulting in softening of the microstructure within the FZ and HAZ, as compared to the AC polarity case. From the above observations, it can be deduced that welding with AC polarity had provided the highest hardness of the weldment due to the evenness in the distribution of heat input to the electrode and plate.

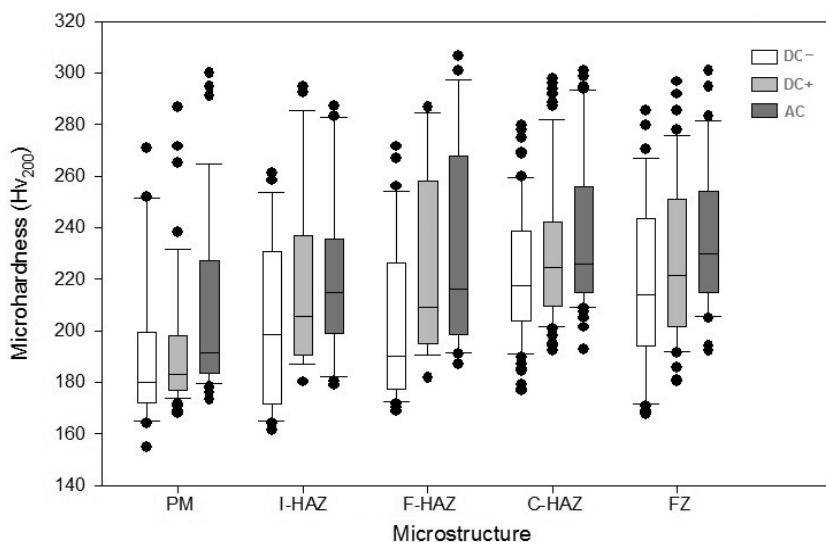
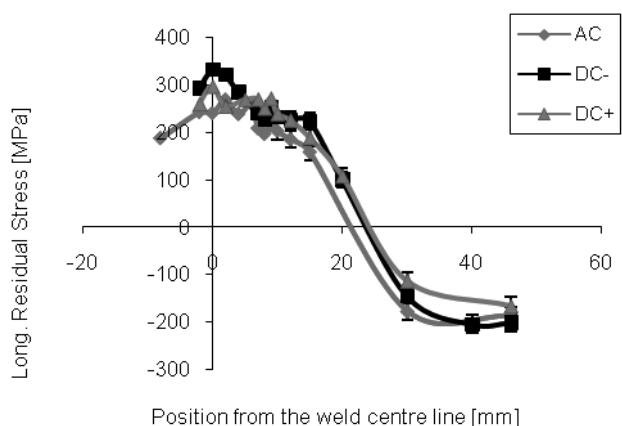


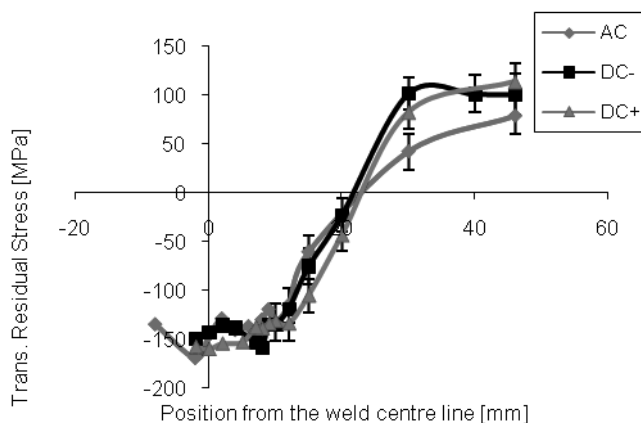
Fig. 7. Box plot representing statistical distribution of the microhardness for different types of microstructures found in the weld samples.

### Residual stresses

Neutron diffraction measurements were made following the guidelines presented in ISO/TTA 3, (2001); D.C.I.T. 21432, (2005). Figure 8 shows the surface (across the weld) residual stress distributions for the samples, which were welded using the DC-, DC+ and AC polarities, respectively. It should be noted that the measurements were made along line 1 (Fig. 2b) that is located 2 mm below the top surface of the plate. Hence, the measurements through the weld significantly represent the HAZ. A close look at the longitudinal residual stress measured across the weld (Fig. 8a) shows that maximum tensile stress occurs near the center of the weld for all samples; this was compensated for by the compressive residual stress in the parent metal away from the weld.



(a)



(b)

**Fig. 8.** Across-the-weld measurements of the residual stresses along: a) longitudinal direction, and b) transverse direction. Measurements are made along line 1 located 2mm below the top surface of the plate as shown in Fig.2b.

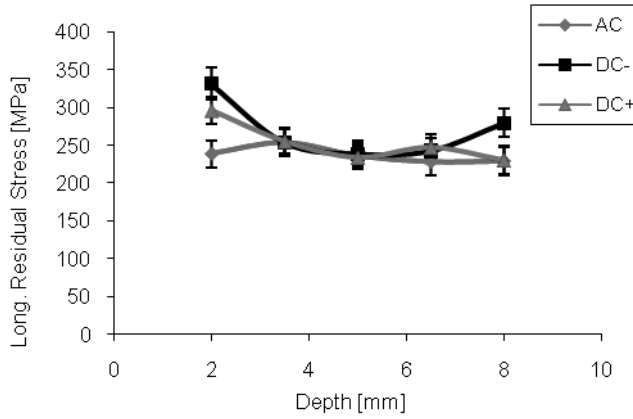


It also shows that at the center of the weld, the sample with DC- polarity has the highest stress value of  $346 \pm 10$  MPa, while the lowest value of residual stress occurs for the AC polarity sample with the magnitude of  $245 \pm 10$  MPa. In addition, the distribution of transverse residual stress shown in Fig. 8(b) looks similar for all welding samples. Compressive residual stresses (around  $-150 \pm 10$  MPa) for all samples were found in, and nearby, the area of the weld. However, further away from the weld (approximately 22-25 mm), the transverse residual stress becomes tensile, reaching the maximum of  $102 \pm 8$  MPa at 30mm (Fig. 8b) for the sample with DC- polarity sample. The residual stress distribution for DC+ polarity is very similar to that of the DC-, within the error bars. On the other hand, AC polarity showed the lowest transverse residual stresses across the weld of  $74 \pm 8$  MPa at 45 mm. It is believed that the transverse residual stress will then relax towards the edge of the sample. Transverse stresses are very important for the design of welded components as, usually, the in-service stresses will superimpose on residual stresses in this particular direction.

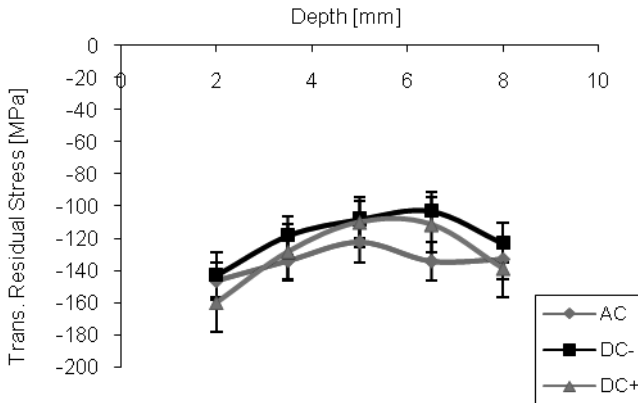
Figure 9 presents the-through-thickness residual stress distributions for the weld samples. It should be noted that the measurements were made along line 2 (Fig. 2) located at the center of the weld, which starts 2 mm below the top surface of the plate towards the bottom of the plate. Hence, the measurements along line 2 mainly represent the HAZ. The longitudinal stress distribution is shown in Fig. 9(a), indicating that DC polarity samples have the highest tensile stresses near the FZ ( $335 \pm 15$  and  $320 \pm 20$  MPa for DC- and DC+ polarity samples, respectively) and become less towards the bottom of the HAZ. The AC polarity sample shows almost constant tensile residual stress of  $240 \pm 15$  MPa in the longitudinal direction for all points of measurements. In addition, Fig. 9(b) shows distribution of transverse residual stresses and indicates that the stresses are compressive throughout the thickness, with the AC polarity sample maintaining the minimum compressive stresses ( $-130 \pm 10$  MPa) at most of the points.

The AC polarity sample has shown to provide the minimum tensile residual stresses in the HAZ, as shown via through-thickness and across the weld measurements. Figure 10 shows the comparison of the residual stresses measured in the three directions (longitudinal, transverse, and normal) for the AC polarity sample. Results from across the weld measurements, shown in Fig. 10(a), indicate that the HAZ (up to 10 mm from the weld center) has the largest tensile residual stress of an average of 250 MPa in the longitudinal direction; this is consistent in magnitude with the results for the through-thickness measurements, as presented in Fig. 10(b). Similarly, the average magnitude of compressive residual stress in the HAZ ( $-150$  MPa) in the transverse and normal direction is consistent with that obtained in the through-thickness case. In general, the distribution of residual stress for the AC

polarity sample reveals that the HAZ has approximately constant residual stresses in all directions of ND measurements. Besides providing the highest microhardness, it can further be deduced that the evenness in the distribution of heat input to the electrode and plate by AC polarity welding caused relatively homogeneous heating and cooling cycles throughout the HAZ and, thus, resulted in constant residual stresses in the weld.



(a)



(b)

**Fig. 9.** Through-thickness measurements of the residual stresses along: a) longitudinal direction, and b) transverse direction. Measurements are made along line 2 located at the center of the weld as shown in Fig.2b.

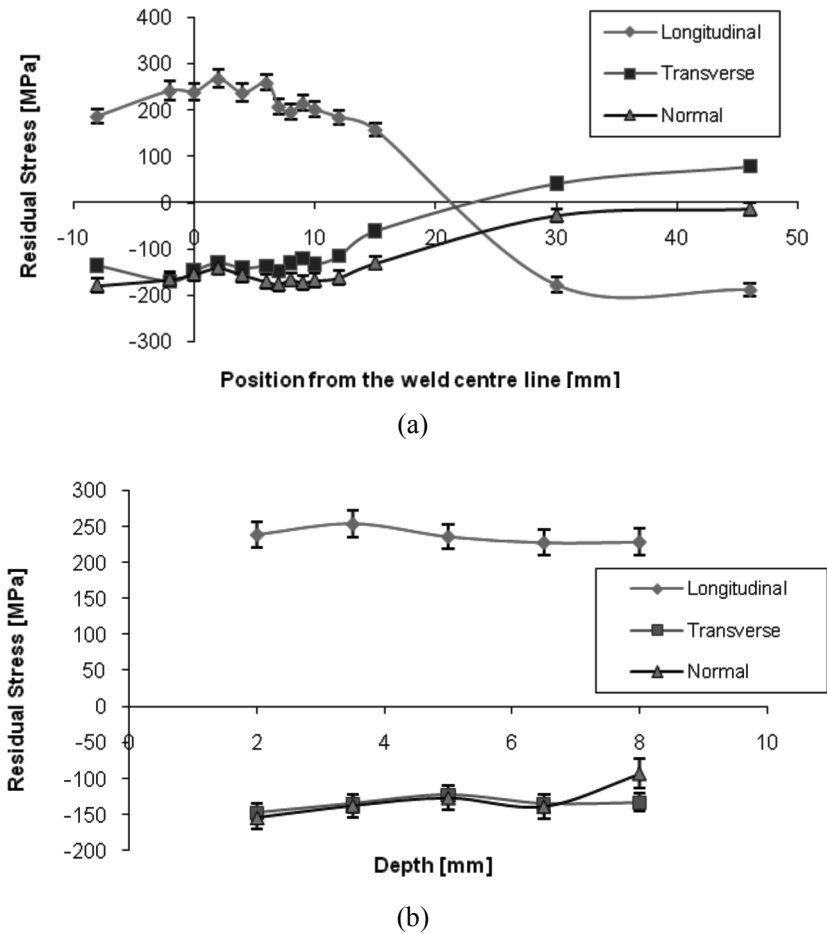


**Fig. 10.** Distribution of residual stresses for AC polarity sample for measurements: a) across the weld, and b) through thickness.

### Heat input of welding polarity

Alternating the amount of heat input by changing the welding polarity has caused different distribution of temperature in the weld and parent metal during the heating and cooling cycles and, thus, has affected on the evolution of microstructure and microhardness. This was also shown to make some differences in the distribution of residual stresses in the weld area, particularly in the HAZ. Recent work by Boumerzoug et al. (2011) examined the thermal cycle of the welding process in low carbon steel AISI 1005 using a weld thermal cycle simulator and made a comparison with a weld joint of the same material by using SMAW. For simulated joints with peak temperature between 600–780°C, spheroidization and coarsening of the lamellar cementite were found to occur, similar to that observed in the intercritical region of the HAZ. Fine and coarse ferritic and pearlitic structures were formed at peak temperatures of 950°C and

1100°C, respectively. Different microstructure was identified by increasing the peak temperature to 1250°C, which looks similar to the microstructure at the bottom region of the FZ observed in the current study. It was also indicated that similarities between the structures of welded joints and of simulated joints exist in terms of constituents and grain size. Boumerzoug et al. (2011) added that the microhardness escalates by increasing the simulation peak temperature from 600°C to 780 °C, and then slightly decreases with the formation of fine ferritic and pearlitic structures at 950°C. With the further increase in peak temperature, the microhardness increases to maximum value at 1250°C. Moreover, Gharibshahiyan et al. (2011) investigated the effect of heat input on the HAZ and grain growth of low carbon steels and showed that, at high heat input and low cooling rate, nucleation and recrystallization occur fast in the HAZ that was found to accelerate grain growth and, hence, results in a reduction of the hardness. It was also observed that increasing the heat input reduces the amount of pearlite that was formed in the HAZ upon cooling. Gharibshahiyan et al. (2011) added that cooling from high temperatures contributes to less grain nucleation and, thus, more tendencies to the formation of ferrites than that of pearlites. In such a case, the ferrite phase nucleates and grows, most likely from the grain boundaries in the form of Widmanstätten.

The aforementioned works, hence, provide strong evidence that varying the heat input to the weld area has an influence on microstructure and microhardness evolution. This is also relevant to the current work for which a different amount of heat input was applied by varying the welding polarity. In particular, it was observed that the locations of intercritical, fine and coarse grained HAZ microstructure vary by changing the polarity and, consequently, caused variation in microhardness (see Figs. 5 and 6). In addition, neutron diffraction measurements of residual stresses have shown that alternating the amount of heat input resulted in different distribution of residual stresses within the HAZ, particularly near the FZ interface (at a depth of 2 mm) as shown in Fig. 9(a). Based on the measurements along the longitudinal direction, the AC polarity sample was found to provide minimum tensile residual stresses and also equal stress distribution in the HAZ. It is anticipated that the evenness in the amount of heat input by AC polarity to the plate and electrode has caused homogenous heating and cooling cycles within the HAZ and, thus, provided approximate constant residual stresses in the HAZ. Despite the microhardness being the maximum for the AC polarity sample, as presented in Figure 7, its median value has slightly changed at different regions of the HAZ. This indicates that the AC polarity sample has more tendencies to develop homogeneous distribution of residual stresses within the weld; since, approximately similar heat input was applied to the electrode and plate.

To summarize, varying welding polarity has been shown to produce some differences in the bead geometry, particularly the bead width and the size of the HAZ,

but it had limited effect on the type of microstructures developed in the weld area. Hence, no significant differences were made on enhancing the microhardness and on lowering the residual stresses of 1020 steel weld. From the above findings, if the residual stress is a critical issue, then a post-weld heat treatment may be necessary for this type of steel weld.

## **CONCLUSIONS**

The effect of heat input as a function of welding polarities (AC, DC- and DC+) was examined on the bead geometry, microstructure, microhardness and residual stresses of SMAW 1020 carbon steel. The following conclusions can be drawn:

1. Welding polarity has significant effect on the bead geometry. DC- polarity provides the maximum bead width and HAZ, highest welding dilution, but the least weld bead height.
2. All weld samples contain similar weld microstructures; the HAZ consists of three regions of intercritical, fine-grained and coarse-grained ferritic and pearlitic microstructures, while the FZ contains coarse columnar dendrites of hard acicular and Widmanstätten ferrites near the fusion line to the weld center and equiaxed dendrites in the upper region bead.
3. Microhardness measurements indicate that the sample with DC- polarity has the lowest values in all regions of the weld. The long thermal exposure of the DC- polarity welding to the plate provided a coarser and softer microstructure in the HAZ, in comparison with DC+ and AC polarities.
4. Across-the-weld measurements show tensile longitudinal residual stresses in the HAZ, for all samples, which were balanced by compressive stress away from the weld. Through-thickness measurements in the longitudinal direction indicate that the DC- polarity sample has the highest tensile residual stress near the FZ interface ( $335 \pm 15$  MPa), while it is the lowest for AC polarity case  $240 \pm 15$ .
5. Even distribution of heat input by AC polarity was found to provide the lowest differences in microhardness and residual stresses within the HAZ.

## **ACKNOWLEDGEMENTS**

The authors wish to gratefully acknowledge the support and use of the CTS welding workshop and Kuwait University General Facility project (GE 01/07) for the use of their facilities with regard to sample preparation, optical metallography and scanning electron microscopy. The authors would also like to register their appreciation of the use of ISIS Pulsed Neutron and Muon Source of the Science and Technology

Facilities Council, Didcot, UK. Special thanks also go to Mr. Paul Curcio from the Maintenance Technology Institute at Monash University, Australia for his assistance in microstructural analysis. Finally, the authors are also indebted to Eng. Abdulaziz Albannay for his help in producing all the welding samples.

## REFERENCES

- Apps, R.L., Gourd, L.M., and Nelson, K.A. 1963.** Effect of welding variables upon bead shape and size in submerged arc welding. *Welding Metal Fabrication* 31(11): 453.
- Boumerzoug, Z., Raouache, E., and Delaunois, F. 2011.** Thermal cycle simulation of welding process in low carbon steel, *Materials Science and Engineering A*, 530: 191–195.
- Chakravarti, A.P., Thibau, R., and Bala, S.R. 1985.** Cooling characteristics of bead-on-plate welds. *Met. Constr. (March)*, 178R–183R.
- Chandel, R.S., Seow, H.P., and Cheong, F.L. 1996.** Effect of increasing deposition rate on the bead geometry of submerged arc welds. *Journal of Materials Processing Technology* 72(1): 124-128.
- D.C.I.T. 21432 2005.** Non-destructive testing. Standard test method for determining of residual stresses by neutron diffraction, DD CEN ISO/TS 21432. British Standards Institute.
- Gharibshahiyan, E., Raouf, A.H., Parvin, N., and Rahimian, M. 2011.** The effect of microstructure on hardness and toughness of low carbon welded steel using inert gas welding. *Materials and Design* 32: 2042–2048.
- Gill, E.T. and Simons, E. N. 1950.** *Modern Welding Techniques*. Sir Issac Pitman and Sons Ltd., London.
- ISO/TTA 3:2001 2001.** Polycrystalline materials - Determination of residual stresses by neutron diffraction.
- Elmer, J.W. and Palmer, T.A. 2006.** In-Situ Phase Mapping and Direct Observations of Phase Transformations during Arc Welding of 1045 Steel. *Metallurgical and Materials Transactions A* 37: 2171-2182.
- Jackson, C.E. 1960** The Science of Arc Welding. Part III - What the Arc Does. *Welding Journal* 1960 39(4): 225-230.
- Jang, J.-i., et al. 2003.** Assessing welding residual stress in A335 P12 steel welds before and after stress-relaxation annealing through instrumented indentation technique. *Scripta Materialia* 48(6): 743-748.
- Jefferson, T.B. 1951.** *The Welding Encyclopedia*. McGraw-Hill, New York.
- Kou, S. 2003.** *Welding metallurgy*. 2nd ed. John Wiley and Sons, Hoboken, New Jersey, USA.
- Lorentzen, T. and Ibs, J.B. 1995.** Neutron diffraction measurements of residual strains in offshore welds. *Materials Science and Engineering A* 197(2): 209-214.
- Messler, J.R.W. 2004.** Welding as a Joining Process, in *Joining of Materials and Structures*. Butterworth-Heinemann, Burlington. Pp. 285-348.
- Nagesh, D.S., and Datta, G.L. 2002.** Prediction of weld bead geometry and penetration in shielded metal-arc welding using artificial neural networks. *Journal of Materials Processing Technology* 123(2): 303-312.
- Owen, R.A., et al. 2003.** Neutron and synchrotron measurements of residual strain in TIG welded aluminium alloy. *Materials Science and Engineering A* 346(1-2): 159-167.

- Pang, J.W.L., et al. 2003.** Effects of tooling on the residual stress distribution in an inertia weld. *Materials Science and Engineering A* 356(1-2): 405-413.
- Paradowska, A., et al. 2005.** A neutron diffraction study of residual stress due to welding. *Journal of Materials Processing Technology* 164-165: 1099-1105.
- Paradowska, A., et al. 2006.** Investigation of reference samples for residual strain measurements in a welded specimen by neutron and synchrotron X-ray diffraction. *Physica B: Condensed Matter* 385-386(Part 2): 904-907.
- Paradowska, A., et al. 2006.** Residual stress measurements by neutron diffraction in multibead welding. *Physica B: Condensed Matter* 385-386(Part 2): 890-893.
- Price, J.W.H., et al. 2008.** Comparison of experimental and theoretical residual stresses in welds: The issue of gauge volume. *International Journal of Mechanical Sciences* 50(3): 513-521.
- Price, J.W.H., et al. 2006.** Residual stresses measurement by neutron diffraction and theoretical estimation in a single weld bead. *International Journal of Pressure Vessels and Piping* 83(5): 381-387.
- Samuels, L.E. 1980.** *Optical Microscopy of Carbon Steels*. American Society for Metals, Metals Park, Ohio.
- Webster, G.A. and Wimpory, R.C. 2001.** Residual stress in weldments. *Journal of Neutron Research* 9(2): 281 - 287.
- Webster, J., et al. 2002.** Measurement and modeling of residual stresses in TIG weld. *Applied Physics A* 74: 1421-1423.
- Yang, L.J., Chandel, R.S., and Bibby, M.J. 1992.** The effects of process variables on the bead width of submerged-arc weld deposits. *Journal of Materials Processing Technology* 29(1-3): 133-144.

**Open Access:** This article is distributed under the terms of the Creative Commons Attribution License (CC-BY 4.0) which permits any use, distribution, and reproduction in any medium, provided the original author(s) and the source are credited.

**Submitted:** 12-03-2014

**Revised:** 19-10-2014

**Accepted:** 19-10-2014